Air Separation and N_2 Purification with $Ba_{0.15}Sr_{0.85}FeO_{3-\delta}$ via a Two-Step Thermochemical Process

H. Evan Bush[c], Matthew Kury, Zachary Berquist, Tania Rivas, Madeline Finale, Kevin Albrecht, and Andrea Ambrosini

Concentrating Solar Technologies, Sandia National Laboratories, Albuquerque, NM USA 87185-1127

[c] - Corresponding Author: H. Evan Bush, Email: hebush@sandia.gov Phone: +1.505.284.1237

Abstract

Thermochemical air separation to produce high-purity N_2 was demonstrated in a vertical tube reactor via a two-step reduction-oxidation cycle with an A-site substituted perovskite $Ba_{0.15}Sr_{0.85}FeO_{3-\delta}$ (BSF1585). BSF1585 particles were synthesized and characterized in terms of their chemical, morphological, and thermophysical properties. A thermodynamic cycle model and sensitivity analysis using computational heat and mass transfer models of the reactor were used to select the system operating parameters for a concentrating solar thermal-driven process. Thermal reduction up to 800 °C in air and temperature-swing air separation from 800 °C to minimum temperatures between 400 and 600 °C were performed in the reactor containing a 35 g packed bed of BSF1585. The reactor was characterized for dispersion, and air separation was characterized via mass spectrometry. Gas measurements indicated that the reactor produced N_2 with O_2 impurity concentrations as low as 0.02% for >30 min of operation. A parametric study of air flow rates suggested that differences in observed and thermodynamically predicted O_2 impurities were due to imperfect gas transport in the bed. Temperature swing reduction/oxidation cycling experiments between 800 and 400 °C in air were conducted with no statistically significant degradation in N_2 purity over 50 cycles.

Keywords: Thermochemical air separation, solar chemical looping, solar reactor, perovskite oxide, strontium ferrite

1 Introduction

Solar thermochemical (STC) processes enable the utilization of concentrated solar irradiation to drive heat transfer, energy storage and release, and/or the production or purification of chemical products. In STC reduction/oxidation (redox) cycles with perovskite metal oxides $ABO_{3-\delta}$ (where A, B represent one or more site-specific metal cations and δ is oxygen non-stoichiometry), the endothermic thermal reduction of metal cations in the perovskite lattice stores absorbed sunlight as a chemical potential and releases stored oxygen via bulk diffusion of O^{2-} anions, creating oxygen vacancies V_O. The stored solar energy is then released via exposure to O_2 (*e.g.,* in air) or other oxygen-containing gases (*e.g.,* $H_2O_{(v)}$, CO_2) to produce a chemical product and/or perform work, and to fill V_O and recycle the $ABO_{3-\delta}$ for later use. These chemical reactions are summarized as:

$$\mathrm{ABO}_{3-\delta} + \Delta H\left(\delta,\Delta\delta,T\right) \leftrightarrow \mathrm{ABO}_{3-\delta-\Delta\delta} + \frac{\Delta\delta}{2}\mathrm{O}_{2(g)} \tag{1}$$

where A and B are generic metal species and ΔH represents the enthalpy of reaction, where a positive ΔH implies solar energy storage in $ABO_{3-\delta}$ for thermal reduction (forward reaction) and energy release from $ABO_{3-\delta}$ for oxidation (backward reaction).

Many perovskites are repeatedly reducible/oxidizable and have high anionic conductivities (with oxygen permeation fluxes of ~10^{-7} mol·cm^{-2}·s^{-1} measured for $SrFe_{0.2}Co_{0.8}O_{3-\delta}$ (Qiu et al., 1995)), which enable rapid reaction rates that are appealing for solar-driven processes. The redox extent δ for a given compound readily changes as a function of temperature and pressure in the range $0 < \delta < 0.5$, where greater δ implies greater reduction extent and V_O formation. Selecting specific conditions to operate a STC cycle controls the change in redox extent $\Delta\delta$ and therefore the total energy and oxygen exchange. These perovskites are well-suited to high-temperature STC redox cycles, as they can be optimized to operate at specific redox temperatures and pressures that are advantageous from a systems perspective and can be rapidly cycled between end conditions to enable a high rate of energy utilization and/or chemical production.

The perovskite $SrFeO_{3-\delta}$ is thermodynamically appealing for removing O_2 from air to produce nearly-pure N_2, which may be of interest for gas commodity production or as a reactant for ammonia synthesis (Vieten et al., 2016). The $SrFeO_{3-\delta}$ ΔH is low compared to more strongly-bound O^{2-} in perovskites studied for processes such as STC H_2/CO production (McDaniel et al., 2014; R. Barcellos et al., 2018; Scheffe et al., 2013) or energy storage (Babiniec et al., 2015, 2016). In these processes, the thermodynamics of the overall H_2/CO_2 splitting reactions and the necessity for dense energy storage motivate increasing the ΔH, whereas for STC air separation the goal is maximizing the product gas output per unit energy of concentrated sunlight. The O^{2-} in $SrFeO_{3-\delta}$ is sufficiently bound to resist over-reduction between ambient and temperatures well above 800 °C but weakly bound enough to promote high air O_2 removal capacity ($\Delta\delta$) per unit solar energy input.

In prior work, La and Ba were identified as A-site substituents which increased the air O_2-removal capacity of $SrFeO_{3-\delta}$ for A-site fractions up to 0.2 (Farr et al., 2020). A compound energy thermodynamic modeling characterization of $A'_xSr_{1-x}FeO_{3-\delta}$ (Bush et al., 2021), where A = Ba, La and $0 \leq x \leq 0.2$, elucidated the equilibrium δ dependence on T, p_{O_2}, and x. The model defined partial redox Gibbs energy, enthalpy, and entropy relationships and enabled identification a range of compositions which enabled optimization of the material to cycle conditions. Kinetics characterizations of $(Ba,La)_{0.15}Sr_{0.85}FeO_{3-\delta}$ and $Sr_{0.85}FeO_{3-\delta}$ (Nguyen et al., 2021) revealed rapid redox rates in powder and pelletized material samples and suggested that the materials were heat and mass transfer limited under the studied temperatures, p_{O_2} conditions, and heating rates.

Conventionally, air separation to purify gas streams is performed in an energy-intensive cryogenic process, including the compression and liquefication of air (Banaszkiewicz et al., 2014), followed by distillation to separate air constituents. Alternatives include pressure- and/or temperature-swing adsorption (PSA and/or TSA) (Banaszkiewicz et al., 2014; Hassan et al., 1986), which are limited in the attainable N_2 purity, and specialized membranes (Kosinov et al., 2016), which are typically more suitable for the removal of minority air constituents such as CO_2.

The STC air separation process is equivalent or similar, on a chemical reaction process basis, to existing cycles and applications which are classified variously as chemical looping air separation (CLAS) (Dou et al., 2019; Görke et al., 2020; Krzystowczyk et al., 2020), chemical looping with oxygen uncoupling (CLOU) (Azimi et al., 2013), high-temperature oxygen sorption (Yang et al., 2002), thermochemical oxygen pumping (Bulfin et al., 2019; Ermanoski and Stechel, 2020), and air-free or chemical looping combustion (CLC) (Falcón et al., 2002). Binary transition metal oxides have been investigated as working materials, in which the selected metal is heavily dependent on the intended operation temperature (Moghtaderi, 2010; Wang et al., 2013). $SrFeO_{3-\delta}$ and substituted compositions are of particular interest, as evidenced in the afore-cited works, due to the stability, rapid kinetics, and continuous redox behavior afforded by nonstoichiometric perovskite oxides.

STC air separation differs from other applications in that it inherently operates partially or exclusively via a temperature swing, whereas other cycles may rely on an isothermal pressure swing for reasons of practicality. STC air separation is also distinguished by the highly directionally and spatially variable nature of a concentrating solar input, which introduces thermal gradients that have unique implications for solar receiver and reactor heat transfer and design, even for off-sun, downstream reactor components such as a decoupled air separation reactor. While non-solar CLAS may operate near-isothermally, a process using moving particles heated in a solar receiver may necessitate a temperature gradient, and thus benefit from using the largest possible extent of the temperature range.

STC air separation with $SrFeO_{3-\delta}$ particles has been demonstrated with a horizontal tube furnace reactor (Bulfin et al., 2019) and was reported to produce inert gases at $p_{O_2} < 10^{-5}$ bar from air without performance degradation over five cycles, with thermal reduction performed at 800 °C and air separation/oxidation at 350 °C. The authors additionally demonstrated air separation from inert gas containing 1% O_2 and suggested a two-stage process in which the product of a PSA system is further purified via STC air separation.

A benchtop vertical packed bed reactor (VPBR), reported herein, was designed, modeled, fabricated, and experimentally operated to demonstrate a two-step redox cycle for STC air separation with $Ba_{0.15}Sr_{0.85}FeO_{3-\delta}$. (BSF1585). The VPBR held an annular packed bed of BSF1585 mounted in a vertical tube furnace which separated high purity N_2 from air via a temperature swing. The system performance was validated by multiphysics reaction models which captured the VPBR tube and reacting bed utilizing coupled chemical properties determined in prior work (Bush et al., 2021; Nguyen et al., 2021).

2 Reactor Design and Construction

The VPBR is shown in Figure 1. A packed bed of approximately 35 g of reactive particles was contained within an annular cavity created by inserting a 24” open-ended alumina tube (1/8” OD, 1/32” wall thickness) into a closed end alumina tube (1/4” ID, 1/8” wall thickness). Sweep gas was introduced by two mass flow controllers (MFC; ALICAT MC-XSCCM-D, X = 200, 500) and entered through the inner tube, flowed through the bed, and continued through the annular region to the reactor outlet. The tube was mounted in the heated zone of a vertical tube furnace (LINDBERG BLUE M HTF55122A).

Temperatures were measured at the gas inlet and within the particle bed by K-type thermocouple probes interfaced via NPT feedthroughs. Two thermocouples positioned outside the tube within the heated zone of the furnace were used for furnace control and measurement, respectively. Pressure drop across the bed was tracked by a differential pressure transducer (DWYER 616D-5). Gas composition was measured downstream of the reactor via a residual gas analyzer (RGA, SRS UGA200) pre-calibrated using a 100 ppm O_2 calibration gas. Gas flow exited the system through a two-stage bubbler assembled from 250 mL Erlenmeyer flasks: the first, empty, to prevent backflow due to system temperature changes and the second, filled with water, to seal the system from the environment.

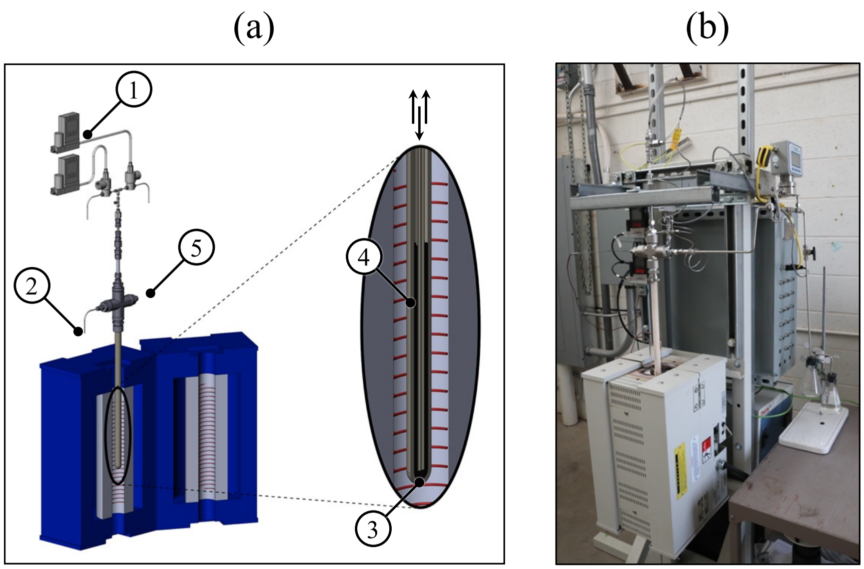

Figure 1. (a) Schematic and (b) photo of the packed bed tube furnace reactor including: (1) mass flow controllers, (2) thermocouple feedthrough, (3) bed thermocouple position, (4) particle bed, and (5) gas outlet. The configuration of inlet/outlet flow in the annular tube is indicated by the arrows.

3 Reactor Modeling

3.1 Materials selection and thermodynamic cycle modeling

The STC media for the VPBR were selected based upon a prior down-selection effort in which the A-site constituent metals Ba, Ca, and La and the B-site constituent metals Cr, Cu, Co, and Mn were experimentally evaluated for their potential to enhance the oxygen non-stoichiometry of $SrFeO_{3-\delta}$ (Farr et al., 2020), itself a well-characterized perovskite oxide with appealing thermochemical air separation thermodynamics (Vieten et al., 2016). While up to 20% Ca, Ba, and La A-site substituents and up to 20% Co B-site doping all enhanced the redox activity of $SrFeO_{3-}$

$_{\delta}$, the composition space was down-selected to the $(Ba,La)_xSr_{1-x}FeO_{3-\delta}$ family. The choice was made due to evidence of phase changes during cycling observed in Ca-substituted samples (Capstick et al., 2023; Farr et al., 2020; Luongo et al., 2020), which can in some cases negatively impact physical and chemical performance over repeated cycles, and the relative cost, environmental, social, and health considerations of Co extraction (Fu et al., 2020).

A thermodynamic air separation cycle analysis was performed to define the optimal air separation operating conditions and $(Ba,La)_xSr_{1-x}FeO_{3-\delta}$ material composition for the cycle. The idealized system, shown in Figure 2, was defined to provide an upper bound on the performance of a two-step solar thermochemical air separation cycle driven by a temperature swing between an on-sun thermal reduction step and an off-sun air separation step. The thermodynamic model, the assumptions and parameters of which are described in detail in (Bush et al., 2019), was adapted from the prior analysis to include particle-particle and particle-gas heat recuperation and the thermodynamics of $(Ba,La)_xSr_{1-x}FeO_{3-\delta}$. Model predictions suggested atmospheric pressure operation of the solar reactor, thermal reduction temperatures of 800 °C and below, and material compositions of $(Ba,La)_{0.15}Sr_{0.85}FeO_{3-\delta}$ were optimal in terms of the attainable N_2 purity and total cycle efficiency. While Ba and La substitution were comparable on a N_2 yield and solar input energy basis, a final down-selection, to $Ba_{0.15}Sr_{0.85}FeO_{3-\delta}$ (BSF1585), was made based on a roughly 85% substituent cost savings on an elemental basis by using BaO versus La_2O_3 as a precursor for a scaled-up process.

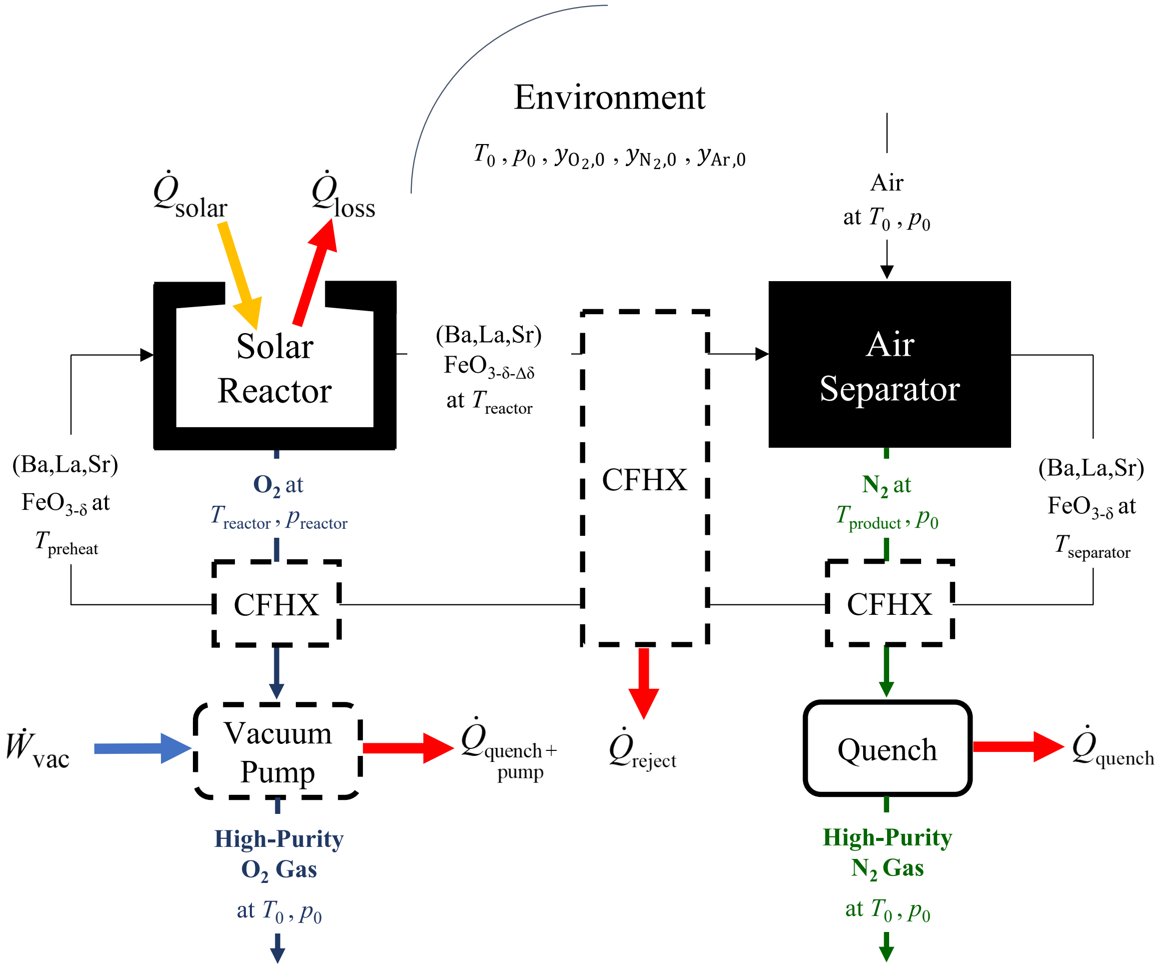

Figure 2. Idealized solar thermochemical air separation process used to define the operating condition range for the vertical packed bed tube reactor.

3.2 Reactor heat and mass transfer modeling

Computational heat and mass transfer models of the VPBR were developed in the SIERRA simulation suite (Team, 2022a, b) to inform the reactor design. The thermodynamic redox properties of BSF1585 were coupled to these models to capture the impacts of the thermal reduction and oxidation reactions on heat and mass transfer. The 2D, axisymmetric VPBR domain, shown in Figure 3, consisted of three regions: 1) the inner and outer solid alumina tubes, which were discretized using the conventional Galerkin finite element method (GFEM) solving the conservation of energy equation, with heat transfer from the furnace to the VPBR approximated as a prescribed temperature schedule on the external boundary; 2) the particle bed, which was modeled with porous mixture models for mass and enthalpy conservation for the solid and gas phases, with a Darcy's Law representation of the gas velocities though the bed, and which was discretized using a control volume finite elements method (CVFEM); and 3) the inlet and outlet of the VPBR, which were approximated as constant temperature injection (mass flow rate) and open (pressure) boundary conditions, respectively, immediately before/after the corresponding surfaces of the particle bed.

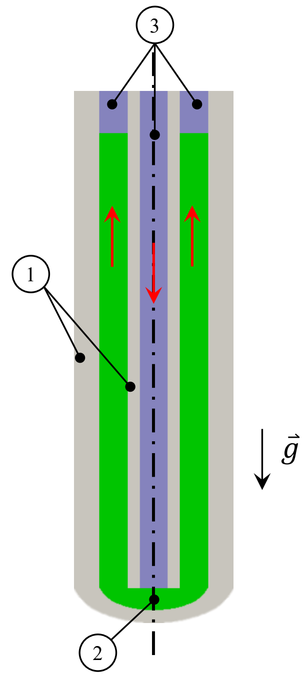

Figure 3. Model domain for the N_2 separation reactor indicating 1) solid tube region, 2) reactive region of BSF1585 particles, 3) and gas inlet/outlet boundaries (not to scale).

Reduction and oxidation of the BSF1585 were modeled as rapid onset Arrhenius-type reactions, represented as:

$$Y_{\mathrm{O}} = k_0 \exp\left(-\frac{E_{\mathrm{a}}}{RT}\right)\left[\delta_{\mathrm{equil}}\left(p_{\mathrm{O}_2}, T\right) - \delta\left(Y_{\mathrm{O}}\right)\right] \tag{2}$$

where R is the ideal gas constant and where the pre-exponential factor k_0 and activation energy E_{a} were tuned to produce near-equilibrium conditions, consistent with the results of kinetic analyses (Nguyen et al., 2021), for the temporal discretization scheme. The Arrhenius temperature dependence was modified by the difference between the equilibrium delta values predicted by the CEF model δ_{equil} and the δ values of the particles from the preceding simulation steps to correctly scale the oxygen source rate terms Y_{O}. The δ_{equil} were calculated from a polynomial surrogate model fitted to CEF results as a function of normalized (T, p_{O_2}). The δ were represented as a linearization of the expected delta values based on the mass fraction of oxygen present in the solid phase. The polynomial forms of δ and δ_{equil} allowed for stable implementation into the numerical chemistry solvers without significant accuracy losses.

To determine the key thermophysical and operating parameters for the VPBR, defined in Table 1, sensitivity analyses were performed on the VPBR model in Dakota (Adams, 2018). The relative sensitivity of the separated N_2 purity to each parameter was reported as the first order Sobol index generated from a polynomial chaos expansion fit to the predicted N_2 purity. The Sobol indices provided a ranked scale of the model inputs in terms of their influence on model outputs.

Table 1. Parameter definitions for the independent thermophysical and operational variables from the model sensitivity study.

Symbol	Definition
T_{reac}	Reactor wall temperature
T_{ref}	Ambient temperature
$\dot{V}$	Injection volumetric flow rate
δ_0	Initial δ value
ΔH	Heat of reaction
k_{eff}	Particle bed conductivity

In general, the VPBR operational variables were more impactful on the system performance than the BSF1585 material properties. As shown in Figure 4, the VPBR was most sensitive to the reactor wall temperature, initial BSF1585 nonstoichiometry, and input air volumetric flow rate. The higher sensitivity to parameters unrelated to BSF1585 chemical properties stemmed from the rapid kinetics of the nonstoichiometric redox reactions, which effectively produced a continuous but sharp “on-off”-like chemical behavior. Therefore, the model was more sensitive to characteristics which directly impacted whether a larger reaction was thermodynamically favorable for a given time-step *(e.g.*, T_{reac}, $\dot{V}$) than to those which did not or only did indirectly (*e.g.,* k_{eff}, ΔH). For materials with more discrete but gradually activated reactions, such a pattern would not necessarily be expected.

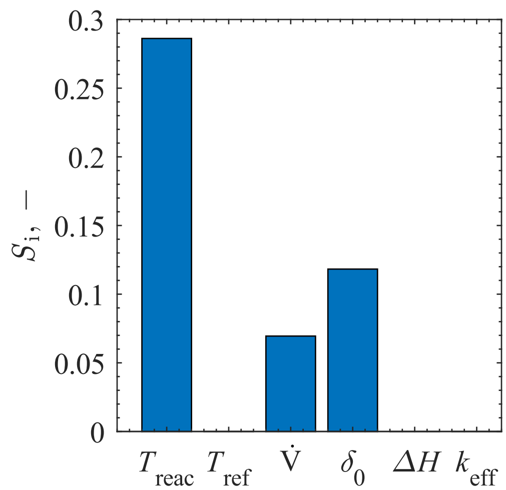

Figure 4. Sobol indices from the model sensitivity study on the independent variables defined in Table 1.

The relative sensitivity of the VPBR to operational parameters and insensitivity to material properties was an advantageous finding, as it enabled resilience of the optimal reactor design to uncertainties in the physical, thermal, and thermochemical properties of the BSF1585, as well as potential future compositional changes (*i.e.,* thermodynamic/kinetic "tuning") of the material.

4 Experimental

Thermal reduction and oxidation experiments were performed in the VPBR to demonstrate the air separation process and compare to model predictions. BSF1585 particles were synthesized via solid state methods and installed in the heated zone of the reactor. Gas transport in the system was then characterized to validate the reliability of gas measurements in estimating the air separation effectiveness. A calibration procedure was developed to correlate raw ionic current measurements from the RGA to concentrations of O_2 and N_2 in the system. Finally, parametric and cycling studies were performed in the reactor to demonstrate thermochemical air separation under a range of conditions.

4.1 Particle synthesis

BSF1585 was synthesized using solid state methods. $BaCO_3$, $SrCO_3$, and Fe_2O_3 were weighed in stoichiometric amounts (metals basis) and placed in a 250 mL PTFE bottle halfway filled with 5 mm YSZ grinding media. The bottle was filled with ethanol until it covered the powders and grinding media. The mixture was ball-milled at 15 Hz for 24 h, removed from the bottle, dried, and calcined in Al_2O_3 crucibles at 700 °C for 8 h, re-ground, and sintered at 1250 °C for 24 h. X-ray diffraction (XRD) performed post-synthesis, shown in Figure 5, confirmed a single phase composition of BSF1585, and thermogravimetric analyzer (TGA) experiments confirmed consistent redox extents with the prior thermodynamic characterization (Bush et al., 2021). To inform the modeling validation studies, several physical and thermal properties of the synthesized BSF1585 were measured or estimated and are reported in Table 2.

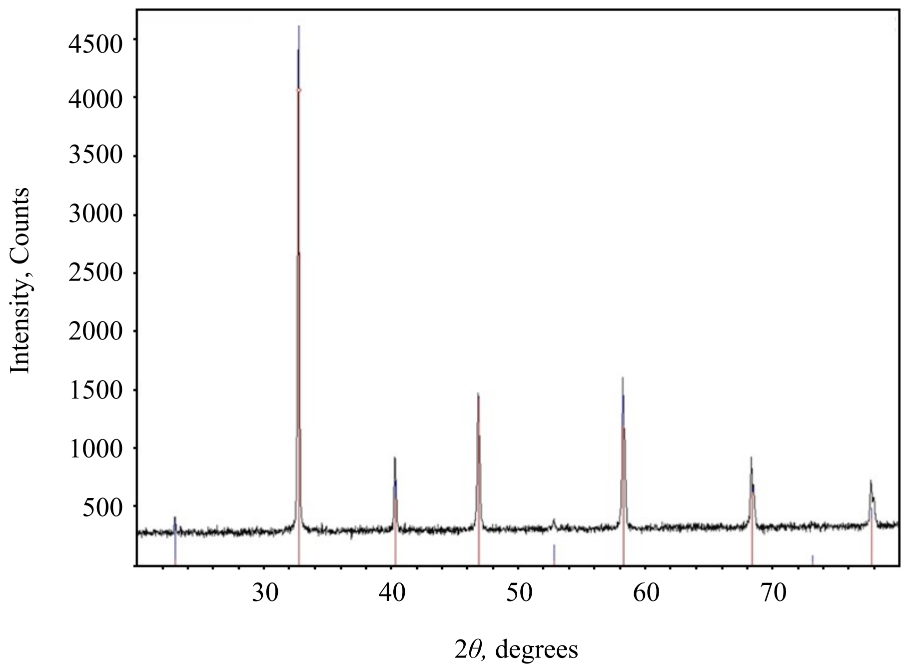

Figure 5. X-ray diffraction pattern of $Ba_{0.15}Sr_{0.85}FeO_3$, indexed to cubic $SrFeO_3$ (PDF #04-002-6497).

Table 2. Thermophysical properties of BSF1585 particles used in tube furnace reactor, including the modeling, estimation, or measurement method used to obtain them.

Property	Units	Value	Method
Particle density	$kg \cdot m^{-3}$	5420	Pycnometry measurement
Bulk density	$kg \cdot m^{-3}$	3319	Porous bed model
Particle heat capacity	$J \cdot mol^{-1} \cdot K^{-1}$	117-125	Debeye theory estimate
Particle thermal conductivity	$W \cdot m^{-1} \cdot K^{-1}$	5	Literature estimate
Bed solar absorptance	–	0.85	410-Solar measurement
Bed total emittance	–	0.91	ET-100 measurement
Mean particle diameter	µm	82	Optical microscopy

The particle size was determined by analyzing optical microscope (LEICA DMS 1000) images of a subsample of 231 particles, as shown in Figure 6a, using the system image processing tool. As shown in Figure 6b, the BSF1585 particles were approximately log-normally distributed with a significant percentage of fines. The particles were sieved to > 53 μm prior to installation in the reactor to reduce the potential for bed fluidization or entrainment.

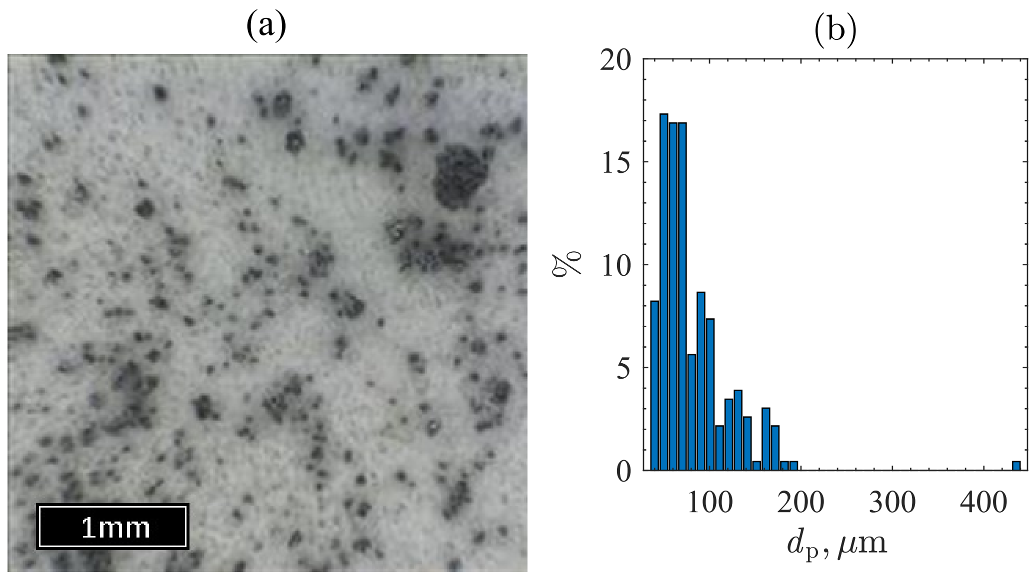

Figure 6. (a) Image of a sample of 231 BSF1585 particles with (b) the corresponding particle diameter size distribution histogram.

4.2 Dispersion characterization

A dispersion characterization was performed to characterize reactor gas transport and correct downstream RGA/O_2 sensor concentration measurements C_{RGA} to estimate gas evolution profiles C_{O_2}, which were implicitly defined as:

$$C_{RGA}(t) = \int_{t'} C_{O_2}(t-t')E(t')dt' \tag{1}$$

where E is the residence time distribution and t' is an integration variable ranging from 0 to t at each instance in time. The $E(t)$ was determined by performing a series of 10 tracer studies in which step changes in gas were input to the reactor, and the inlet (reported by the MFC) and outlet (measured by the RGA) profiles were compared temporally to capture dispersion. The average of the ten outlet profiles, along with the 95% confidence intervals estimated from a t-distribution and the computed standard deviation at each timestep, are shown in Figure 7a. The step changes logged by the MFCs were found to take place on ~0.01 s and were therefore approximated as ideal step profiles relative to the sampling resolution of the RGA (~3 s).

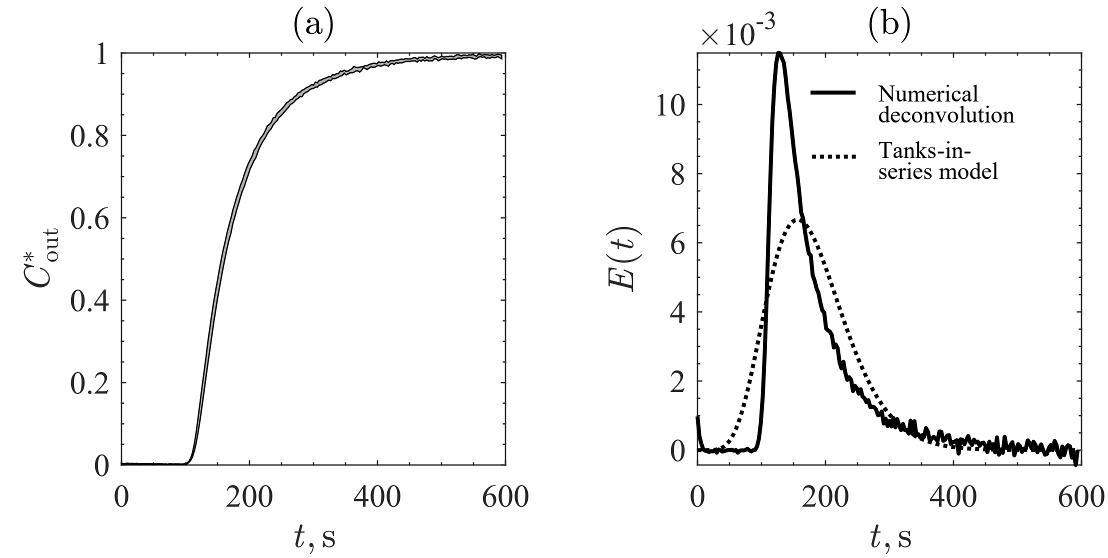

Figure 7. (a) Average tracer output concentration as measured by the residual gas analyzer, normalized from 0 to 1, for 10 replicates, represented as a *t*-distributed 95% confidence band; (b) residence time distributions estimated via two methods: numerical deconvolution (solid line) and a fitted continuously stirred tanks in series model (dashed).

The numerically deconvoluted $E(t)$ was calculated from the average inlet and outlet profiles and is reported in Figure 7b as a solid line. A lag of roughly 90 s was observed in the tracer experiments, and the average residence time of gas was 179 s. The deconvolved $E(t)$ sharply rose above 0 at approximately 100 s, consistent with the increase in C^*_{out} in Figure 7a at the same time. A continuously stirred tanks in series model (Levenspiel, 1999) with eight tanks was also fit to the average tracer profile as an independent validation of the numerical determination and is shown as a dashed line. While the mean of the fitted $E(t)$ was close to the deconvolved value, the fitted model overestimated the variability of gas residence time, demonstrating the difficulty of the model-fitting method in characterizing systems as they approach plug flow. The deconvolved $E(t)$ was therefore used for the dispersion correction. The C_{RGA} values were corrected to obtain C_{O_2} values in the same numerical manner as for calculating $E(t)$. The numerical methods for the deconvolution were defined fully in (Bush et al., 2017).

4.3 Calibration

At the beginning of each air separation experiment, RGA data was obtained to perform a six-point calibration, as shown in Figure 8, from raw ionic current to gas concentration. The two mass flow controllers were used to input flows of air and a calibration gas of 100 ppm O_2 in balance N_2, respectively, at defined percentages from 0 to 100% calibration gas, with the same volumetric flow rate as the successive experiment. Each of the first five steps, depicted in the first 100 min of Figure 8 for one experiment, were performed for 10 min to allow for equilibration. For the final step with 100% calibration gas, the step length was extended to 45 min or more to ensure residual air was purged from the system. The final 30 s of data from each step was used to calculate an average ionic current datapoint. Two-dimensional 95% error bars for the gas volumetric flow rates and ion current were calculated from the variation in the measured signals from the mass flow controllers and RGA, respectively, over this period. A second order polynomial was fit to the known gas concentrations to the average ionic currents for O_2 and N_2 via nonlinear least squares regression to produce gas concentration calibration curves.

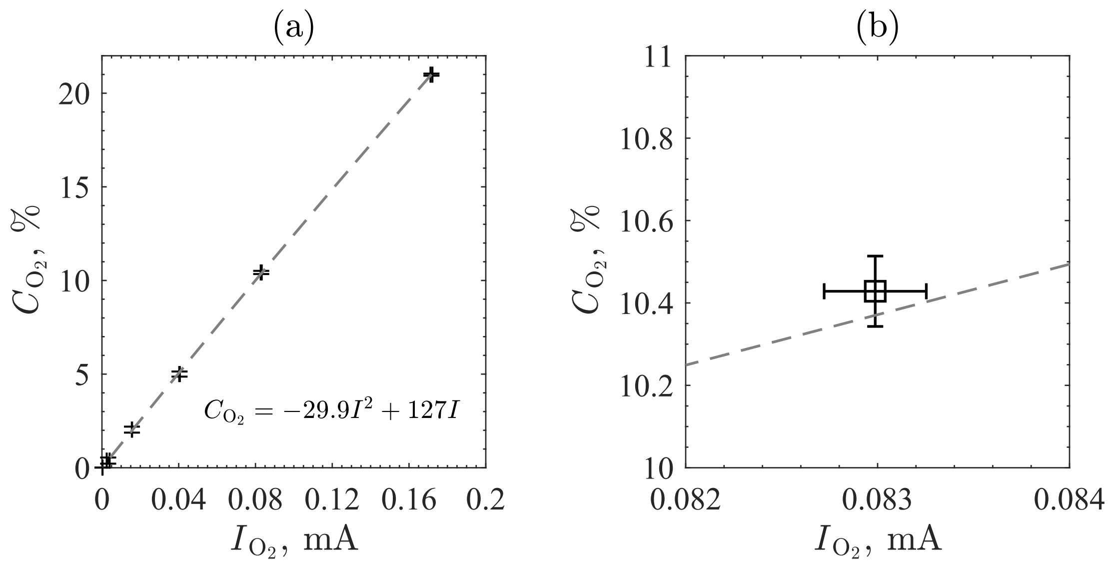

Figure 8. (a) O_2 ionic current measurements and the corresponding estimated O_2 concentration (error bars) for the six-point calibration procedure, fitted to a second-order polynomial calibration curve; (b) detail view of the error measurement and fitted curve near the 10% O_2 datapoint, with two-dimensional error bars.

4.4 Air separation experiments

Air separation was performed using BSF1585 at a range of thermal reduction temperatures and temperature swings ΔT to understand the impact on the VPBR air separation effectiveness and duration. The air separation was allowed to proceed immediately at the beginning of the cooldown stage to avoid parasitic energy requirements or enhanced thermal reduction which could occur from vacuum pumping and/or an inert purge. Non-isothermal air separation also captured the conditions of a solar-heated, countercurrent, moving particle process, where the highest temperature particles entering the reactor immediately "polish" the lowest O_2 concentration gas exiting the reactor. While the bed was stationary for the experiments, the rates of air separation observed during the ΔT compared to an ideal (*i.e.,* heat/mass transfer limited) process were relevant to the design of a moving system.

An example air separation experiment with a thermal reduction temperature T_{red} = 800 °C, followed by air separation during a cooldown to a minimum temperature T_{sep} = 400 °C, is shown in Figure 9. Following the RGA calibration from t = 0 to 100 min, a volumetric air flowrate $\dot{V}$ = 40 mL·min^{-1} was introduced, and the furnace was heated at 10 K·min^{-1} to T_{red}, followed by a 120 min dwell to allow for thermal reduction and the purge of product O_2 from the system. The furnace was then cooled at ≤ 20 K·min^{-1} to T_{sep}, followed by an 80 min dwell to allow for complete reoxidation of the bed and separation of O_2 from the air sweep. The spike in relative O_2 before t = 200 min was from the thermal reduction of the bed, and a rapid drop in O_2 between 300 and 400 min characterized the continuous separation of N_2 from air until the bed O_2 removal capacity was depleted, *i.e.*, the BSF1585 was completely reoxidized.

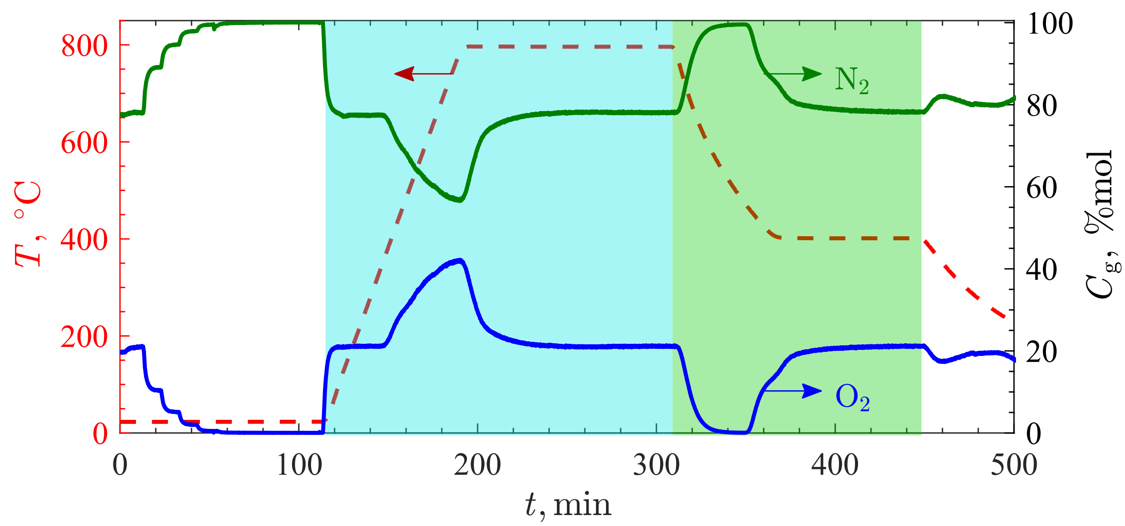

Figure 9. Air separation experimental summary, including calibration (first from left, white shaded), thermal reduction (next, blue shaded), air separation (next, green shaded), and post-experiment cooldown (last, white shaded) steps. Gas concentration measurements (bold lines) are overlaid on furnace temperature (dashed line).

Pressure variation influences on the RGA signal prevented a precise integration of the total molar O_2 release and recovery via the calibrated gas concentration signals. However, the relative integrated areas for the two reaction regions in Figure 9 confirmed that the total O_2 release during reduction was larger than the O_2 separated during cooldown, consistent with expectations for the relative temperature/pressure conditions of the bed. The O_2 exchange during air separation was roughly estimated to be 82% of the O_2 released during thermal storage. Thermodynamically, a ratio of 52% was expected for BSF1585 for the experimental conditions (Bush et al., 2021). Uncertainty in the baseline concentration impacting the area of the "tails" of the curves likely contributed to the difference. Low temperature kinetic limitations on the initial BSF1585 nonstoichiometry may have also played a role.

A parametric study of air separation was performed at $\dot{V}$ = 40 mL·min^{-1}, T_{red} = 600, 700, and 800 °C, and T_{sep} = 400, 500, and 600 °C, as the prior thermodynamic material and cycle analyses indicated these were the temperature ranges of interest for the process (Bush et al., 2021). A second parametric study was performed for T_{red} = 800 °C, T_{sep} = 400 °C, and $\dot{V}$ = 20, 30, and 40 mL·min^{-1} to analyze whether nonidealities in transport of air through the packed bed impacted the separation process. A multi-cycle study, also at T_{red} = 800 °C, T_{sep} = 400 °C, was conducted, during which 50 successive reduction/air separation steps were performed to evaluate the repeatability of the process.

5 Results and Discussion

A detailed view of the air separation step from the experimental summary in Figure 9 is shown in Figure 10. The rapid transitions in the C_{O_2} profile as soon as the bed began to cool until T_{sep} was reached suggested that the reaction was heat and mass transfer limited, as in the prior kinetic analysis of BSF1585 (Nguyen et al., 2021), meaning that the oxidation state of the particle bed was limited by the rate of cooling and that at each temperature "step" the bed was oxidized from beginning to end in a moving front (rather than uniformly, like in a well-mixed reactor). This observation was consistent with the finding that dispersion in the system was not severe. A minimum O_2 concentration $\lfloor C_{O_2} \rfloor$ = 0.05% ± 0.01% was measured during the air separation step, which was several orders of magnitude higher than the air separation effectiveness predicted by the heat and mass transfer model with coupled BSF1585 thermodynamics.

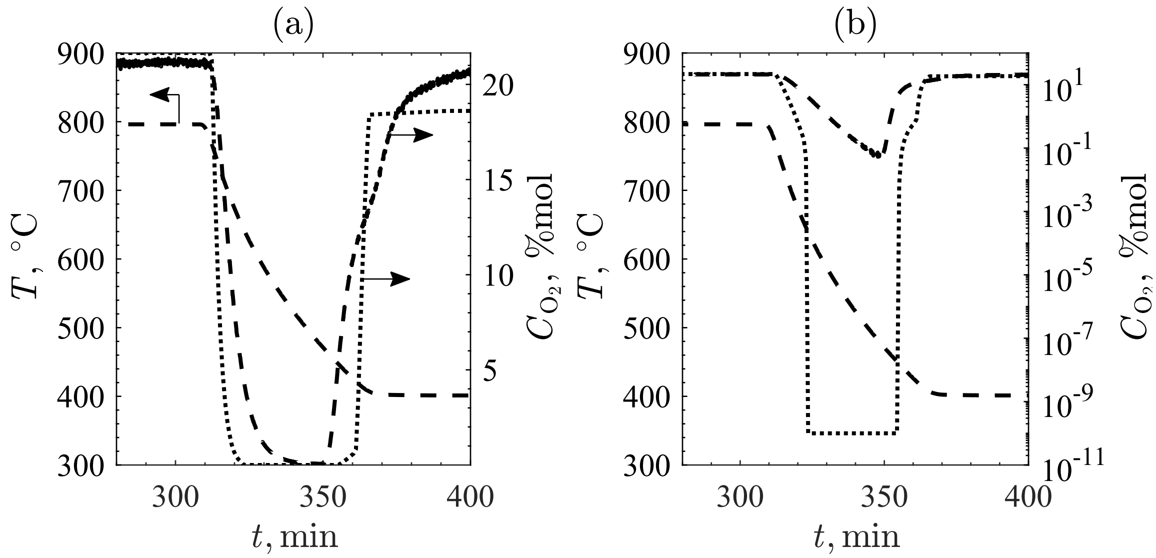

Figure 10. Air separation step of the experiment shown in Figure 9. Experimental (solid line) and modeled (dotted) oxygen concentrations are overlaid on furnace temperature (dashed) on (a) linear and (b) log scales.

The VBPR air separation results are aggregated in Figure 11a in terms of the $\lfloor C_{O_2} \rfloor$ observed in the separation phase and Figure 11b in terms of total duration of the separation phase Δt, defined as the time elapsed between the onset and cessation of C_{O_2}decrease when the oxygen uptake capacity of the bed was depleted. The Δt was used to characterize the air separation stage rather than an overall N_2 production volume as the air separation was a batch process, where the product N_2 had a variable purity, while a solar implementation would likely be a continuous process, with a constant exiting N_2 purity. The Δt therefore was determined to be a relevant metric for reactor design of a well-insulated, internally cooled, moving bed of particles.

The bar plots are grouped as a function of reduction and separation temperature. Both C_{O_2} values and error bars are plotted on a logarithmic scale. While no isothermal experiment was performed, T_{red} = 600 °C, T_{sep} = 600 °C bars of $\lfloor C_{O_2} \rfloor$ = 20.95% and Δt = 0 min are shown in Figure 11a and b as references.

More complete air separation and longer air separation durations were both associated with a larger ΔT due to the greater average $\Delta\delta$ between the reaction steps. More complete and longer separation was also associated with higher T_{red} for equal values of ΔT, which may have resulted from higher cooling rates in the higher T_{red} experiments enabling more O_2 removal capacity for the flowing air sweep. While the furnace was programmed to allow cooling up to 20 K·min^{-1}, the thermal inertia of the system resulted in rates peaking around 14, 11, and 9 K·min^{-1} for T_{red} = 800, 700, and 600 °C, respectively.

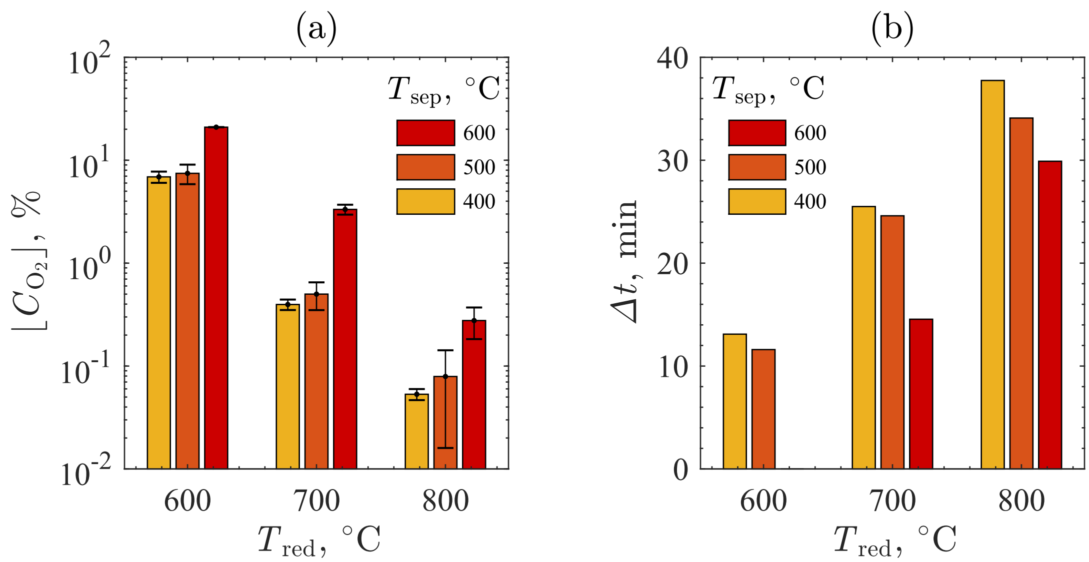

Figure 11. Bar graphs for air separation performed at combinations of three reduction and three air separation temperatures in terms of (a) minimum attained O_2 concentration and (b) total duration of the air separation stage.

The $\lfloor C_{O_2} \rfloor$ as a function of volumetric flowrate for T_{red} = 800 °C, T_{sep} = 400 °C air separation experiments are plotted in Figure 12. For experiments at $\dot{V}$ < 40 mL·min^{-1} air, there was a statistically significant decrease in $\lfloor C_{O_2} \rfloor$, to a minimum of $\lfloor C_{O_2} \rfloor$ = 0.02% ± 0.01% for the 20 mL·min^{-1} experiment, suggesting that there was some nonideality in the flow of the air sweep through the packed bed (*e.g.,* tunneling, bypassing of flow near walls), which likely explained a significant portion of the higher-than-predicted $\lfloor C_{O_2} \rfloor$ measurements in the parametric temperature study compared to the model results. This trend of decreasing $\lfloor C_{O_2} \rfloor$ would be expected to diminish or disappear entirely for a longer and/or more tortuous isothermal packed bed. While decreasing $\dot{V}$ improved the completeness of separation, doing so increased the required purge and equilibration times for the VPBR during experimentation and decreased the relative production rate of high-purity N_2. $\dot{V}$ = 40 mL·min^{-1} was therefore retained as the standard flowrate which maximized production while avoiding bed fluidization and/or particle entrainment.

The $\lfloor C_{O_2} \rfloor$ achieved in the VPBR were an order of magnitude higher than achieved previously in a horizontal packed bed reactor using un-substituted $SrFeO_{3-\delta}$ (SF) (Bulfin et al., 2019), which was likely explained by several factors: SF has a higher oxygen affinity (*i.e.*, is less readily reducible and more readily oxidized) than BSF1585, the horizontal tube was operated at lower temperatures for the air separation step, and the reduction was performed in Ar, all of which increased the $\Delta\delta$ between the reduction and air separation steps, and therefore the air separation capacity of the bed. While use of higher ΔH materials, a sweep gas, and/or significant vacuum pumping would negatively impact the overall thermodynamic efficiency of the cycle, other engineering design measures could be used to increase the N_2 purity of the process, including (1) multi-stage packed or moving metal oxide beds (of differing compositions or at varying temperatures), (2) coupling the VPBR to a process like pressure-swing adsorption, (3) modest variations in the process pressures, and (4) material synthesis and/or channel design strategies to increase the gas-particle contact in the bed.

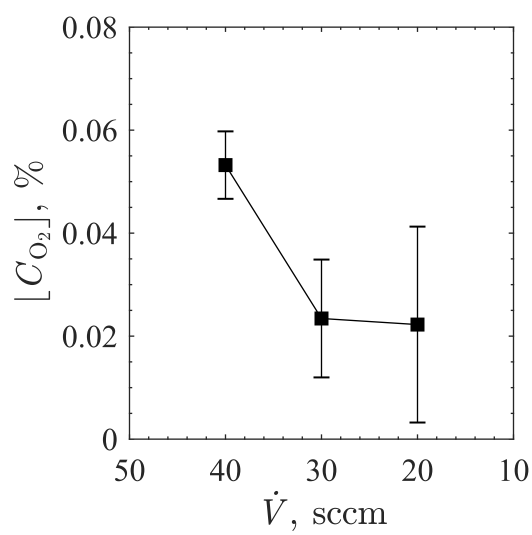

Figure 12. Minimum attained O_2 concentration with 95% confidence intervals as a function of flow rate for three air separation experiments performed at a thermal reduction temperature of 800 °C and an air separation temperature of 400 °C.

The $\lfloor C_{O_2} \rfloor$ as a function of cycle number for 50 temperature swing air separation cycles at T_{red} = 800 °C, T_{sep} = 400 °C, and $\dot{V}$ = 40 mL·min^{-1} is shown in Figure 13. The air separation effectiveness was highly repeatable after the first several cycles, as the 95% confidence intervals of the $\lfloor C_{O_2} \rfloor$ measurements were consistently overlapping. The initial decay in $\lfloor C_{O_2} \rfloor$ was attributed to the bed starting from a relatively more oxidized state at room temperature and converging upon an increased reduction extent as the excess oxygen was incrementally removed from the bed.

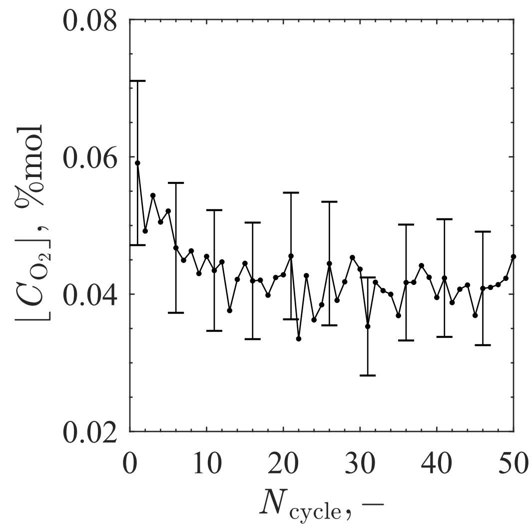

Figure 13. Minimum attained O_2 concentration with 95% confidence intervals as a function of cycle number for 50 air separation cycles performed at a thermal reduction temperature of 800 °C, an air separation temperature of 400 °C, and an air flow rate of 40 mL·min^{-1}.

6 Conclusions

Thermochemical air separation using $Ba_{0.15}Sr_{0.85}FeO_{3-\delta}$ was demonstrated in a vertical packed bed reactor (VPBR) in temperature swing experiments performed in air at atmospheric pressure. Thermal reduction up to 800 °C, which could be reasonably achieved in a concentrating solar receiver/reactor, and air separation performed between 400 and 600 °C were shown to reduce the oxygen concentration in air by more than three orders of magnitude, producing nearly pure N_2 for more than thirty minutes. There was no evidence of decay in the achievable purity of N_2 over 50 cycles performed with the same bed of material. Varying the flowrate of the air sweep suggested that air transport nonidealities in the packed bed caused the N_2 purity to be significantly lower than the level attainable according to BSF1585 chemical thermodynamics. In the future, N_2 purity may be improved via multi-stage processes, coupling to other air separation technologies, and/or reactor designs which optimize particle-gas contact.

Acknowledgements

This material based upon work supported by the U.S. Department of Energy Solar Energy Technologies Office under Award No. DE-EE0001529, Sandia National Laboratories is a multimission laboratory managed and operated by National Technology & Engineering Solutions of Sandia, LLC, a wholly owned subsidiary of Honeywell International Inc., for the U.S.

Department of Energy's National Nuclear Security Administration under contract DE-NA0003525.

Nomenclature

A	perovskite A-site cation
B	perovskite B-site cation
C	gas concentration (molar percent)
E	residence time distribution
E_a	activation energy
H	molar enthalpy of reaction
k_0	Arrhenius pre-exponential factor
N	cycle number
p	pressure
R	ideal gas constant
T	temperature
t	time
V	vacancy; volume
x	A-site Ba^{2+}/La^{3+} substituent molar fraction
Y	gas source rate

Greek Letters

δ	oxygen nonstoichiometry/deviation from stoichiometry
Δ	total change
μ	micro-

Subscripts

0	environmental dead state value
eff	effective bed property
equil	equilibrium
g	gas, gaseous state
O	monotonic oxygen, perovskite oxygen-site anion or vacancy
O_2	(associated with) oxygen

reac	reactor
red	reduction
ref	reference/ambient value
sep	air separation step (in reference to minimum temperature reached)
vac	vacuum pump

Superscripts/Accents

°	degree, standard atmospheric conditions
ʻ	ionic substitution; integration variable indicator
·	time rate of change

Operators

$\lfloor\rfloor$	minimum value

Abbreviations

BSF	Ba-substituted $SrFeO_{3-\delta}$
CFHX	counter-flow heat exchanger
CVFEM	control volume finite element method
GFEM	Galerkin finite element method
ID	inner diameter
MFC	mass flow controller
NPT	national pipe thread
PSA	pressure swing adsorption
PTFE	polytetrafluoroethylene
RGA	residual gas analyzer
SF	$SrFeO_{3-\delta}$
STC	solar thermochemical
TGA	thermogravimetric analyzer
TSA	temperature swing adsorption
VPBR	vertical packed bed reactor
XRD	X-ray diffraction/diffractometer
YSZ	yttria-stabilized zirconia

References

Adams, B.M., Bohnhoff, W.J., Dalbey, K.R., Ebeida, M.S., Eddy, J.P., Eldred, M.S., Frye, J.R., Geraci, G., Hooper, R.W., Hough, P.D., Hu, K.T., Jakeman, J.D., Khalil, M., Maupin, K.A., Monschke, J.A., Ridgway, E.M., Rushdi, A.A., Stephens, J.A., Swiler, L.P., Vigil, D.M., Wildey, T.M., Winokur, J.G., 2018. Dakota, a multilevel parallel object-oriented framework for design optimization, parameter estimation, uncertainty quantification, and sensitivity analysis: Version 6.7 user's manual. Sandia National Laboratories, Albuquerque, NM.

Azimi, G., Leion, H., Rydén, M., Mattisson, T., Lyngfelt, A., 2013. Investigation of different Mn–Fe oxides as oxygen carrier for chemical-looping with oxygen uncoupling (CLOU). Energy & Fuels 27(1), 367-377.

Babiniec, S.M., Coker, E.N., Miller, J.E., Ambrosini, A., 2015. Investigation of $La_xSr_{1-x}Co_yM_{1-y}O_{3-\delta}$ (M = Mn, Fe) perovskite materials as thermochemical energy storage media. Sol. Energy 118, 451-459.

Babiniec, S.M., Coker, E.N., Miller, J.E., Ambrosini, A., 2016. Doped calcium manganites for advanced high-temperature thermochemical energy storage. International Journal of Energy Research 40(2), 280-284.

Banaszkiewicz, T., Chorowski, M., Gizicki, W., 2014. Comparative analysis of cryogenic and PTSA technologies for systems of oxygen production. AIP Conference Proceedings 1573(1), 1373-1378.

Bulfin, B., Lapp, J., Richter, S., Gubàn, D., Vieten, J., Brendelberger, S., Roeb, M., Sattler, C., 2019. Air separation and selective oxygen pumping via temperature and pressure swing oxygen adsorption using a redox cycle of $SrFeO_3$ perovskite. Chemical Engineering Science 203, 68-75.

Bush, H.E., Datta, R., Loutzenhiser, P.G., 2019. Aluminum-doped strontium ferrites for a two-step solar thermochemical air separation cycle: Thermodynamic characterization and cycle analysis. Sol. Energy 188, 775-786.

Bush, H.E., Nguyen, N.P., Farr, T., Loutzenhiser, P.G., Ambrosini, A., 2021. Air separation via a two-step solar thermochemical cycle based on $(Ba,La)_xSr_{1-x}FeO_{3-\delta}$: Thermodynamic analysis. Solid State Ion. 368, 115692.

Bush, H.E., Schlichting, K.-P., Gill, R.J., Jeter, S.M., Loutzenhiser, P.G., 2017. Design and characterization of a novel upward flow reactor for the study of high-temperature thermal reduction for solar-driven processes. Journal of Solar Energy Engineering 139(5), 051004-051004-051011.

Capstick, S., Bulfin, B., Naik, J.M., Gigantino, M., Steinfeld, A., 2023. Oxygen separation via chemical looping of the perovskite oxide $Sr_{0.8}Ca_{0.2}FeO_3$ in packed bed reactors for the production of nitrogen from air. Chemical Engineering Journal 452, 139289.

Dou, J., Krzystowczyk, E., Wang, X., Robbins, T., Ma, L., Liu, X., Li, F., 2019. A and B-site co-doped $SrFeO_3$ oxygen sorbents for enhanced chemical looping air separation. ChemSusChem n/a(n/a).

Ermanoski, I., Stechel, E.B., 2020. Thermally-driven adsorption/desorption cycle for oxygen pumping in thermochemical fuel production. Sol. Energy 198, 578-585.

Falcón, H., Barbero, J.A., Alonso, J.A., Martínez-Lope, M.J., Fierro, J.L.G., 2002. $SrFeO_{3-\delta}$ perovskite oxides: chemical features and performance for methane combustion. Chemistry of Materials 14(5), 2325-2333.

Farr, T.P., Nguyen, N.P., Bush, E., Ambrosini, A., Loutzenhiser, P.G., 2020. An A-and B-Site substitutional study of $SrFeO_{3-\delta}$ perovskites for solar thermochemical air separation. Materials 13(22), 5123.

Fu, X., Beatty, D.N., Gaustad, G.G., Ceder, G., Roth, R., Kirchain, R.E., Bustamante, M., Babbitt, C., Olivetti, E.A., 2020. Perspectives on cobalt supply through 2030 in the face of changing demand. Environmental Science & Technology 54(5), 2985-2993.

Görke, R.H., Marek, E.J., Donat, F., Scott, S.A., 2020. Reduction and oxidation behavior of strontium perovskites for chemical looping air separation. International Journal of Greenhouse Gas Control 94, 102891.

Hassan, M.M., Ruthven, D.M., Raghavan, N.S., 1986. Air separation by pressure swing adsorption on a carbon molecular sieve. Chemical Engineering Science 41(5), 1333-1343.

Koepf, E., Advani, S.G., Steinfeld, A., Prasad, A.K., 2012. A novel beam-down, gravity-fed, solar thermochemical receiver/reactor for direct solid particle decomposition: Design, modeling, and experimentation. International Journal of Hydrogen Energy 37(22), 16871-16887.

Kosinov, N., Gascon, J., Kapteijn, F., Hensen, E.J.M., 2016. Recent developments in zeolite membranes for gas separation. Journal of Membrane Science 499, 65-79.

Krzystowczyk, E., Wang, X., Dou, J., Haribal, V., Li, F., 2020. Substituted $SrFeO_3$ as robust oxygen sorbents for thermochemical air separation: correlating redox performance with compositional and structural properties. Physical Chemistry Chemical Physics.

Levenspiel, O., 1999. Chemical Reaction Engineering, 3rd ed. Wiley.

Loutzenhiser, P.G., Barthel, F., Stamatiou, A., Steinfeld, A., 2011. CO_2 reduction with Zn particles in a packed-bed reactor. AIChE Journal 57(9), 2529-2534.

Loutzenhiser, P.G., Tuerk, O., Steinfeld, A., 2010. Production of Si by vacuum carbothermal reduction of SiO_2 using concentrated solar energy. JOM 62(9), 49-54.

Luongo, G., Donat, F., Müller, C.R., 2020. Structural and thermodynamic study of Ca A- or Co B-site substituted $SrFeO_{3-\delta}$ perovskites for low temperature chemical looping applications. Physical Chemistry Chemical Physics 22(17), 9272-9282.

McDaniel, A.H., Ambrosini, A., Coker, E.N., Miller, J.E., Chueh, W.C., O'Hayre, R., Tong, J., 2014. Nonstoichiometric perovskite oxides for solar thermochemical H_2 and CO production. Energy Procedia 49(0), 2009-2018.

Mo¨ller, S., Palumbo, R., 2000. The development of a solar chemical reactor for the direct thermal dissociation of zinc oxide. Journal of Solar Energy Engineering 123(2), 83-90.

Moghtaderi, B., 2010. Application of chemical looping concept for air separation at high temperatures. Energy & Fuels 24(1), 190-198.

Müller, R., Haeberling, P., Palumbo, R.D., 2006. Further advances toward the development of a direct heating solar thermal chemical reactor for the thermal dissociation of $ZnO_{(s)}$. Sol. Energy 80(5), 500-511.

Nguyen, N.P., Farr, T.P., Bush, H.E., Ambrosini, A., Loutzenhiser, P.G., 2021. Air separation via two-step solar thermochemical cycles based on $SrFeO_{3-\delta}$ and $(Ba,La)_{0.15}Sr_{0.85}FeO_{3-\delta}$ perovskite reduction/oxidation reactions to produce N_2: rate limiting mechanism(s) determination. Physical Chemistry Chemical Physics 23(35), 19280-19288.

Nikulshina, V., Gebald, C., Steinfeld, A., 2009. CO2 capture from atmospheric air via consecutive CaO-carbonation and $CaCO_3$-calcination cycles in a fluidized-bed solar reactor. Chemical Engineering Journal 146(2), 244-248.

Qiu, L., Lee, T.H., Liu, L.M., Yang, Y.L., Jacobson, A.J., 1995. Oxygen permeation studies of $SrCo_{0.8}Fe_{0.2}O_{3-\delta}$. Solid State Ion. 76(3), 321-329.

R. Barcellos, D., Sanders, M.D., Tong, J., McDaniel, A.H., O'Hayre, R.P., 2018. $BaCe_{0.25}Mn_{0.75}O_{3-\delta}$—a promising perovskite-type oxide for solar thermochemical hydrogen production. Energy & Environmental Science 11(11), 3256-3265.

Scheffe, J.R., Weibel, D., Steinfeld, A., 2013. Lanthanum–strontium–manganese perovskites as redox materials for solar thermochemical splitting of H_2O and CO_2. Energy & Fuels 27(8), 4250-4257.

Schrader, A.J., Schieber, G.L., Ambrosini, A., Loutzenhiser, P.G., 2020. Experimental demonstration of a 5 kW_{th} granular-flow reactor for solar thermochemical energy storage with aluminum-doped calcium manganite particles. Applied Thermal Engineering 173, 115257.

Team, S.T.F.D., 2022a. SIERRA Low Mach Module: Fuego User Manual - Version 5.10. United States, p. Medium: ED; Size: 860 p.

Team, S.T.F.D., 2022b. SIERRA Multimechanics Module: Aria User Manual - Version 5.10. United States, p. Medium: ED; Size: 5234 p.

Vieten, J., Bulfin, B., Call, F., Lange, M., Schmucker, M., Francke, A., Roeb, M., Sattler, C., 2016. Perovskite oxides for application in thermochemical air separation and oxygen storage. Journal of Materials Chemistry A 4(35), 13652-13659.

Wang, K., Yu, Q., Qin, Q., 2013. The thermodynamic method for selecting oxygen carriers used for chemical looping air separation. Journal of Thermal Analysis and Calorimetry 112(2), 747-753.

Yang, Z., Lin, Y.S., Zeng, Y., 2002. High-temperature sorption process for air separation and oxygen removal. Industrial and Engineering Chemistry Research 41(11), 2775-2784.